Research Article

Ultrathin tunable conducting oxide films for near-IR applications: an introduction to spectroscopy shape theory

A. L. Villarreal-Rios[1] · Á. H. Bedoya-Calle[2] · F. J. Caro-Lopera[3] · U. Ortiz-Méndez[2] · M. García-Méndez[1] · F. O. Pérez-Ramírez[4]

Received: 18 June 2019 / Accepted: 24 October 2019 / Published online: 5 November 2019

Abstract
We report tunable RF-sputtered AZO nanofilms through of deposition conditions. Perfect adsorption of light was simulated in ENZ mode. The coupling condition of thickness and wavelength in perfect absorption was obtained by a Drude model. The fitted parameters range as follows: charge density, from 1.6×10^{20} to 4.4×10^{20} cm^{-3}; mobilities, from 8.23 to 12.76 $cm^2 V^{-1} s^{-1}$; and resistivities, from 14.20 to 34.98 Ω cm. The so-called spectroscopy shape analysis is introduced for automatic detection of elusive XPS peaks and sample surface-etching classification.

Keywords AZO · UV–VIS · Epsilon-near-zero mode · Perfect absorption · XRD · XPS · Spectroscopy shape analysis · Riemannian distances · Metamaterials

1 Introduction

The conductive transparent oxides (TCOs) in thin films have been of great interest due to the modulation capacity of their optoelectronic properties through the variation of the deposition conditions and post-processing. The TCOs have high transmittance at visible and near-infrared frequencies, and a light doping can produce a quasi-neutral region of charge carrier concentrations between 10^{19} and 10^{20} cm^{-3}, exhibiting a characteristic metallic behavior [1]. Unlike noble metals, TCOs are low-loss materials ($\mathrm{Im}(\epsilon_2) < 0.5$), which are an essential alternative as plasmonic/metasurfaces materials. Materials oxides with epsilon-near-zero (ENZ) ($-1 < Re(\epsilon_1) < 1$) have perfect absorption (PA $>$ 99.9%) with broadband and electronically tunable response so that TCOs with a precise thickness can be used in a vast number of applications such as light-harvesting technologies and high-resolution optical space technologies [2].

ADL [3, 4], DC/RF sputtering [5–8], spray pyrolysis [9], sol–gel [10] among other techniques have been used for the manufacture of oxidized conductive materials. Principal challenges in the fabrication of AZO are its low thermal stability and problems of environmental degradation due to the high reactivity of aluminum [5]. In contrast, the AZO is an economical material due to its abundance in the soil, its low toxicity, and its best properties without additional heat treatment, which saves time and money in the manufacturing process with the possibility of using flexible substrates [11]. All these advantages together make the AZO a candidate for the design of zero-index metamaterials in the near-infrared range, to give some examples: telecommunications [12] and sensors [13].

Electronic supplementary material The online version of this article (https://doi.org/10.1007/s42452-019-1569-y) contains supplementary material, which is available to authorized users.

✉ Á. H. Bedoya-Calle, rigelbach@gmail.com | [1]Facultad de Ciencias Físico Matemáticas, Universidad Autónoma de Nuevo León, San Nicolás de los Garza, México. [2]CIIDIT, Universidad Autónoma de Nuevo León, Apodaca, México. [3]Facultad de Ciencias Básicas, Universidad de Medellín, Medellín, Colombia. [4]Facultad de Ingenierías, Universidad de Medellín, Medellín, Colombia.

This work presents the optical, morphological, and chemical characterization of AZO samples. In general, the data obtained by X-ray photoelectron spectroscopy (XPS) have overlapping peaks that differ in their width, peak shape, and intensity. XPS spectra are also complicated by the presence of X-ray satellites and ghosts, so it is necessary to adjust the curves to extract the chemical information from these data. Although the XPS instrument software includes curve fitting, its misuse leads to erroneous conclusions about surface chemistry [14]. We present a novel spectroscopy analysis based on shape theory ([15] and related works) and cumulative XPS data [16]. The method involves Riemannian distances to compare surface-etching cumulative electron counts within samples. The approach also detects the peaks automatically without any expert chemical knowledge. It also provides an alternative descriptive method for the classical Gaussian mixture analysis for elusive peaks. The analysis concludes a best deposit conditions and the chemical phases presented in the samples under environmental and etching conditions.

2 Experimental

Al-doped ZnO thin films were deposited by RF reactive magnetron sputtering from a metallic circular target (1" diameter, 1/8" thickness) of Zn Al (98%, 2%) alloy in an ultra-high-purity argon atmosphere (98% Molar). The base pressure pumped into the reservoir bell was reached in 5.0×10^{-5} Torr. The gas was introduced through individual electronic mass-flow meters (Alborg). The target/substrate distance was varied in two configurations: a maximum distance of 5 cm (large) and one (small $\approx$ 3 cm) in this interval; a moveable shutter was placed between target and substrate. For all samples, plasma was then generated at a working pressure of between 8 and 10 mT by applying an RF power of 30 W and an argon flow during deposition of 1 sccm followed by five minutes of cleaning by sputtering the target with protection of the shutter to avoid contamination by foreign agents to the material. A quartz crystal oscillator monitored the thickness and deposition rate. In Table 1, growth discharge conditions are summarized.

Optical transmittance and reflectance measurements were performed at the wavelength range of 300 to 2500 nm with a JASCO spectrophotometer. Spectroscopic ellipsometry measurements were collected using a Horiba, Jobin Yvon UVISEL HR 320 ellipsometer.

The structural properties were analyzed by XRD using a Rigaku Miniflex II diffractometer (CuKα radiation). A standard $\theta - 2\theta$ Bragg–Brentano geometry was used for measurements with a step size of 0.02°.

Table 1 The growth discharge conditions for AZO thin films on a glass substrate

Sample	1	2	3
Power (W)	30		
Gas (1sccm)	Argon		
Base pressure (torrs)	$8.5E10^{-5}$		
Rate (Å/s)	1.8	1.8	2.9–3.4
Time (min)	30	13	15
Growth distance	*L*	*S*	*L*

XPS measurements were performed with Thermo Scientific *K* alpha system equipment with monochromatized Al Kα anode (1486.6 eV). Survey and high-resolution (HR) spectra were collected with a resolution of 1 eV and 0.1 eV, respectively, with pass energies of 200 eV and 50 eV. The X-ray beam spot size was 400 μm^2. The binding energies were referenced to neutral adventitious C(1s) peak at 285.0 eV. Measured HR spectra of the Zn(2p), Al(2p), and O(1s) windows were analyzed after a linear background subtraction.

3 Results and discussion

3.1 Optical constants and perfect absorption

The use of semiconductor materials for the development of optical devices in both ultraviolet–visible (UV–Vis) and infrared (IR) ranges has been due to the adjustment of their behavior in the dielectric medium. For this analysis, a 1.1-mm-thick glass substrate was used as an incoherent medium to avoid internal interference due to its difference in thickness compared to the coatings studied here, while the ZnO:Al films are presented as coherent and isotropic media. The effective dielectric medium was calculated from the reflectance adjustment (*R*). At normal incidence, the relationship is fulfilled by $\tilde{r} = (\sqrt{\tilde{\epsilon}} - 1)/(\sqrt{\tilde{\epsilon}} + 1)$ and $R = \tilde{r}\tilde{r}^*$. $A = 1 - R$ relates reflectance *R* and absorptance *A*. As we can see in Fig. 1a, the maximum absorptance was 0.94%, 0.98% and 0.97% located at a wavelength of 992 nm, 1488 nm and 584 nm for the samples of AZO 1, 2 and 3, respectively. In contrast to sample 3, a plateau can be seen in the region of maximum absorption over a range of 900–1360 nm for sample 1 and 1230-1430 nm for sample 2. The standard free-electron Drude model described the complex permittivity around the ENZ wavelength:

$$\epsilon_{\mathrm{AZO}} = \epsilon_{\infty} - \frac{w_{\mathrm{p}}^2}{w^2 + iw\Gamma} \tag{1}$$

where $w_{\mathrm{p}}^2 = \mathrm{Ne}^2/m^*\epsilon_0$ and $\Gamma = e/m^*\mu$. Here e is the elementary charge, m^* the electro-effective mass which we assume constant for our absorptance calculations

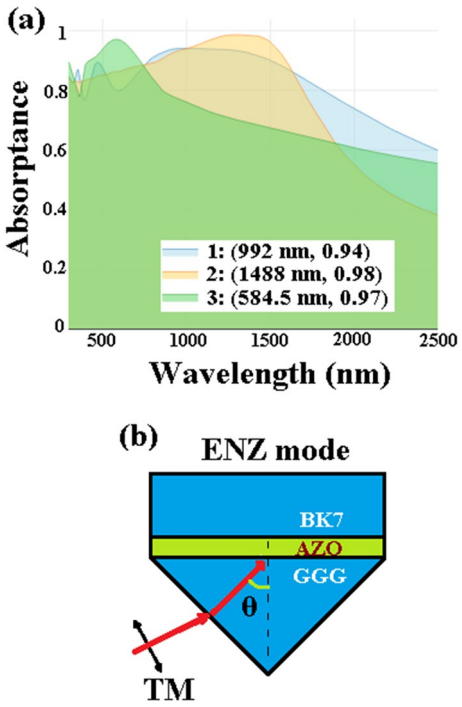

Fig. 1 **a** Maximum experimental absorptance ($A = 1 - R$) at normal incidence for AZO samples 1, 2 and 3, respectively. **b** ENZ mode

Table 2 Optoelectronic's constant on AZO samples

Sample	1	2	3
Thickness (nm)	175	395	150
Energy gap (eV)	3.66	3.68	3.24
N ($\times 10^{20}$ cm^{-3})	1.6	4.4	3.4
μ (cm^2 V^{-1} s^{-1})	10.96	8.23	12.76
ρ ($\times 10^{-4}\,\Omega$ cm)	34.99	17.25	14.20

($m^* = 0.32m_e$) [17], μ is the electron mobility, N is the electrons (charge concentration), ϵ_0 is the permittivity of free space, ϵ_∞ is the permittivity at infinite frequency, w_p is the plasma frequency, and Γ is the electron collision rate. The epsilon-near-zero (ENZ) frequency is defined as Re (ϵ_{AZO}) $= 0, w_{ENZ}^2 = w_p^2/\epsilon_\infty - \Gamma^2$.

For the simulation of a perfect absorption (PA), the values obtained from the adjustment by Drude model will be taken into account, which is summarized in Table 2. For corroborating the validity of modeling of the optical properties via the UV–Vis spectroscopy, the charge concentration calculated through the ellipsometry for samples 1 and 2 was 6.7×10^{20} cm^{-3}, and 3.9×10^{20} cm^{-3}, respectively.

As described in Fig. 1b for a perfect absorption (PA) in ENZ nanolayer mode is required a *p*-polarized (TM) light of wavelength λ incident at a θ angle with a gadolinium gallium garnet (GGG) coupling prism ($n = 1.95$) [18] on an AZO film of the thickness t. If the external medium is a dielectric with the refractive index lower than the GGG prism, for example, a Corning or BK7 glasses, $n \approx 1.54$, the ENZ mode is configured. The Kretschmann–Raether configuration [19] with an angle of incidence above the critical angle was used to excite the ENZ mode. As is well known, the excitation of TM mode leads to an improvement of the electric field confined to the AZO layer and the optical density of the states, resulting in strong absorption of light. To achieve a PA depends on a critical choice of the ENZ wavelength, thickness and angle that satisfies the coupling condition [2]:

$$\frac{2\pi t_{PA}}{\lambda_{PA}} = \frac{(Re(\epsilon_{AZO})^2 + Im(\epsilon_{AZO})^2)}{nggg^3 Im(\epsilon_{AZO})} \sin(\theta_{PA}) \tan(\theta_{PA}) \quad (2)$$

with t_{PA} is the AZO thickness to an PA.

Figure 2 is constructed from filling a 440×440 matrix where the rows correspond to the wavelengths and the columns represent incidence angles, using Eq. (2) to obtain the minimum thickness of maximum absorption. The matrix components represent the optimized thickness for each angle of incidence and each wavelength with it is respectively associated with real and imaginary dielectric constant and the refractive index value of the GGG prism. Results obtained from this analysis show that for both the Drude and Drude–Lorentz models we obtained a single wavelength that optimizes the perfect absorption or thickness. We will take as reference the incidence angle of 50° ± 0.3° close to the critical angle reported for the ITO [2].

Zero permittivity λ_{ENZ} was localized at wavelengths of 1411.13, 1243.32, and 1019 nm for AZO samples 1, 2, and 3, respectively.

As can be seen in Fig. 2, there is an evolution of the perfect absorption band ranging from 1244.5 to 929.5 nm in the Drude model (DM) and from 1489.5 nm to 999.5 nm in the Drude–Lorentz model (DLM). It can also be noted that as we move toward the conditions of sample 3 (Fig. 2), both the Drude and Drude–Lorentz models, the two bands tend to be similar, indicating that the optimal conditions are being reached of growth from AZO nanolayer. By design, the Kretschmann–Raether configuration in ENZ mode exhibits a wavelength PA greater than the wavelength of zero permittivity ENZ ($\lambda_{PA}/\lambda_{ENZ} > 1$) [2]. The wavelengths of complete absorption were located at 1244.5, 1169.5, and 929.5 nm for samples 1, 2, and 3 respectively; therefore, the ENZ mode criterion begins to be partially covered in sample 3 with $\lambda_{PA}/\lambda_{ENZ} \approx 0.91$ for the Drude model and 0.98 for the Drude–Lorentz model.

From the parametric sweep described above, we optimized the thickness of the AZO nanolayer samples and the broadband absorption. We started with real thicknesses obtained through scattering relations which

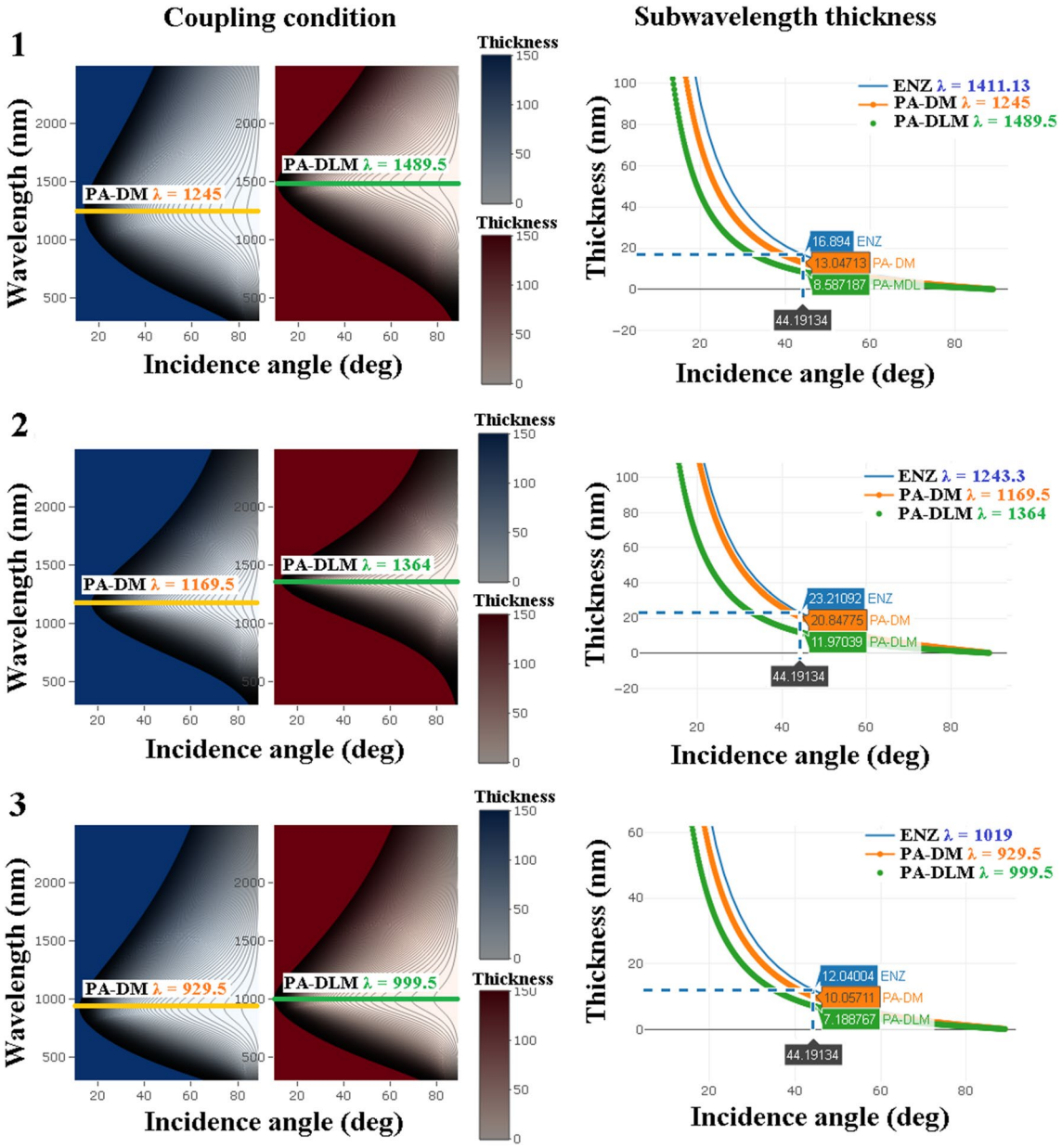

Fig. 2 Critical mode coupling condition (Eq. 2) using Drude model (blue) and by comparison the Drude-Lorentz model (red). The thickness of the optimized AZO nanolayer stack for ENZ mode

values were 175, 395, and 150 nm for samples 1, 2, and 3 respectively; to move on to the optimized thicknesses at 9.62, 15.37, and 7.41 nm at incidence angle of 50° via Drude model in ENZ mode for all three samples respectively, see SI in figure S5.

It is well known that the excitation of the polariton modes leads to an improved electric field confined within the TCO nanolayer of an approximate thickness of λ_{ENZ} /100, in our case, we obtained 16.9, 23.2, and 12 nm for the AZO nanolayer samples 1, 2, and 3, respectively. ENZ mode in subwavelength RF-sputtered AZO nanolayer sample 3 in 12 nm was reached at an incidence angle of 44.2° (see Fig. 2), which compared to the case of the ITO nanolayer was 43.7° with a corresponding thickness of 80 nm [20].

3.2 XRD analysis

Diffraction patterns (θ-2θ) were obtained for samples 1, 2, and 3 (see Fig. 3), and the reflections assignment corresponds to a würzite structure, JCPDS file 79-0207 (a = 3.256 Å, c = 5.212 Å) [21]. Samples 1 and 3 have a highly

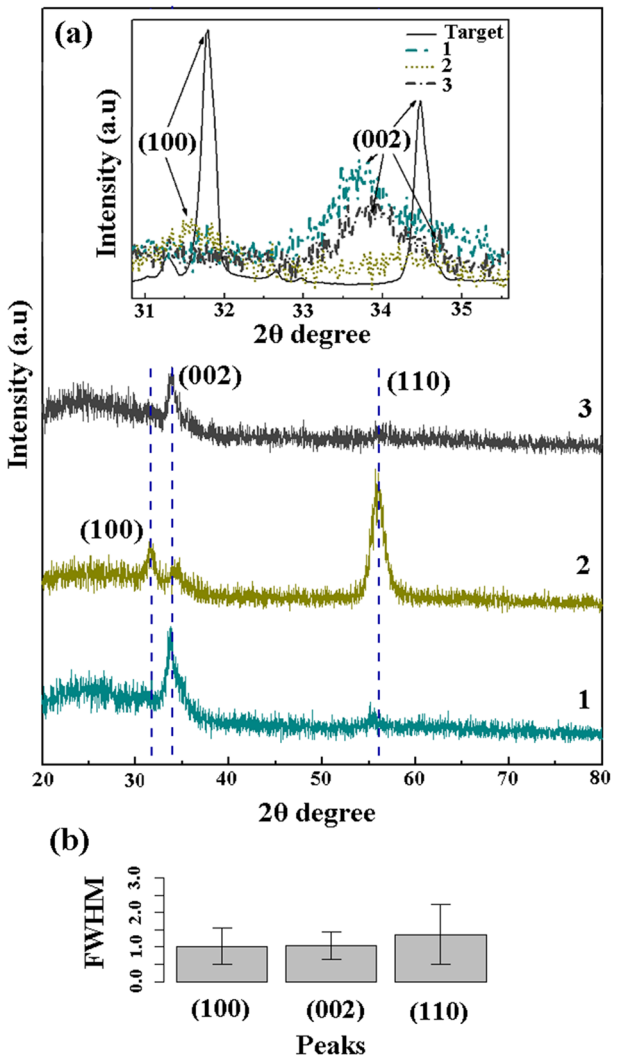

Fig. 3 **a** XRD patterns of the AZO samples and inside: Detail of the deviation in the planes (001) and (002) compared with the pattern in bulk of the material, and **b** error bars in the estimation of peak broadening using Eq. 6

preferred orientation in (002) lattice plane, while that of sample 2 has a major orientation in (110) lattice plane, both orientations have a higher crystalline quality. The most intense (002) reflection indicates growth to the *c*-axis [0002] at perpendicular direction to substrate that yields a tensile biaxal microstrain, the related peaks at 34.38°, and 56.46° correspondings to the (002) and (110) lattice planes in samples 1 and 3 [7, 22, 23]. On the other hand, the (110) orientation plane in the sample 2 has compressive biaxial microstrain, the related peaks at 31.66°, 34.38° and 56.46° correspondings to the (100), (002), and (110) lattice planes produced through a growth that is parallel to the substrate surface.

The instrument correct broadening is related: $\beta_D^2 = \beta_{\text{measure}}^2 - \beta_{\text{instrument}}^2$. Crystallite size broadening may be expressed through the Scherrer equation [24, 25]:

$$D = \frac{k\lambda}{\beta_{\text{D}} \cos(\theta)} \tag{3}$$

where D is the volume average crystallite size, k is a constant depending upon lattice direction and morphology (0.9), λ is the wavelength of CuK α radiation (0.15406 nm), and β_D is the peak breadth due to infinite size. Crystal imperfection and distortion of strain-induced peak broadening are related:

$$\epsilon = \frac{\beta_{\text{S}}}{4 \tan(\theta)} \tag{4}$$

where ϵ is the mean strain and β_S is the peak breadth due to microstrain. In general, instrument broadening function is defined by:

$$\beta_{hkl} = \beta_{\text{D}} + \beta_{\text{S}} \tag{5}$$

$$\beta_{hkl} = \frac{k\lambda}{D \cos(\theta)} + 4\epsilon \tan(\theta) \tag{6}$$

The dispute on oriented growth can be summarized quantitatively through the coefficient of textured (T_c) between addresses (002) to (110) by the following equations:

$$T_c = I(002)/(I(002) + I(110)) \tag{7}$$

and

$$T_c = I(110)/(I(002) + I(110)) \tag{8}$$

where *I(hkl)* is the peak intensity observed in the diffraction patterns [16]. The difference in intensities of the peaks (002) and (110) is due to preferential orientation or textured, that is, the influence that a matrix has on nucleation and / or the growth of new grains in that matrix [26].

3.3 Introducing to spectroscopy shape theory applied to XPS analysis

3.3.1 Modeling spectroscopy curves by using shape theory

The statistical analysis for the AZO samples classification is presented in the supplementary information (SI) in Sect. 3.1. The samples classification is based on the data in survey spectra with a resolution of 1 eV see SI figure S7.

This classification of the samples can be depicted together in the table S1 (see SI), and some conjectures can be proposed in terms of an extreme bootstrap median distance evolution. For example, it seems that there are exclusive zones for elements and some evolution in the samples can be inferred. In O(1s), the samples can be ordered as 2, 3, 1 according to the variable

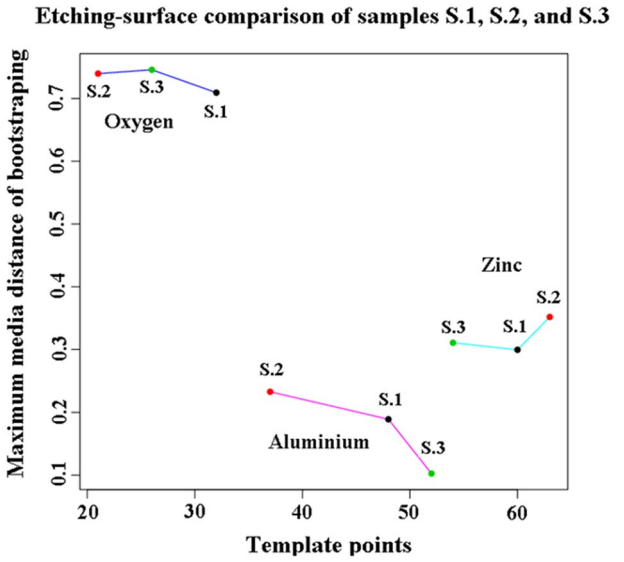

Fig. 4 Bootstrap median distance for O(1s), Zn(2p) and Al(2p). Note that each element tends to occupy an exclusive zone in the plane. A distance between etching and surface also provides the performance of the technique. Smallest distance reflects a well behavior in the corresponding element

parameter in the experiment as a choice in the distance of growth (small or large) target/substrate and of the deposition time of the material, see Table 1. It means that calibration of that parameter in a new experiment in a neighborhood of the conditions of experiment 3 can provide a maximum content of O(1s). In Zn(2p), the calibration tends to give more of that element in the neighborhood of the conditions of experiment 2, with a possible order 3, 1, 2 of the corresponding parameter. Finally, the distance method also detects that conditions around sample 2 give more Al(2p), when the experiment parameter is near to conditions of sample 1; in this case, the favorable order seems to be 3, 1, 2 (see Fig. 4)

3.3.2 Inflection curves

The inflection curves, Sect. 3.2, in the supplementary information material offer a very good approximation of the main peaks and satellite ones with automatic detection.

The peaks detected for O (1s) in AZO samples have traditionally been classified into three regions [8]:

1. High-energy region (532–533 eV) that is attributed to the existence of negatively charged oxygen species, such as $-CO_3$, –OH, adsorbed H_2O or adsorbed O_2 on the surface of AZO films.
2. Medium-energy region (531.08–531.98 eV) is attributed to the O^{2-} ions in the regions of oxygen deficiencies within the ZnO matrix.
3. Low-energy region (529.08–530.98 eV) is corresponding to the O^{2-} ions in the würsite hexagonal structure of the Zn^{2+} array, surrounded by Zn atoms (or substitution of Al atoms) with their full complement of nearest neighbor O^{2-} ions.

A fourth region is detected by the inflection curve method: (4) the left peak of 528 eV in the etching by oxygen samples corresponding to a surprising detection of the Al_3O_3 specimen [27].

As can be seen in the etching oxygen in SI table S6, only the detection of regions (2), (3), and (4) appear which implies that no specimens of the region (1) appear. The detection of a single peak in the region (3) indicates a maximum in the number of oxygen atoms in a full oxidized stoichiometric surrounding while the reduction of electron count in the region (1) or their absence in the samples with etching is an indication of the reduction in the concentration of oxygen vacancies (Table 3).

In the samples without etching or exposed superficially appear the regions (1), (2), and (3), with a particular dispute in the region (1) of the carbon specimens and the deficiencies of O^{2-}in the matrix ZnO of the region (2). An atmospheric doping can affect the materials at different

Table 3 Hexagonal lattice parameters, microstrain, crystallite size, and texture coefficient present in the samples

Sample	Lattice parameters *a* (Å)	*c* (Å)	Microstrain (dimensionless)
1	3.3286	5.3302	5.4×10^{-3}
2	3.2928	5.1691	2.1×10^{-2}
3	3.2978	5.2814	3.8×10^{-2}
Sample	Crystallite size (nm)	Texture coefficient (dimensionless) (002)	(110)
1	8.5	0.71	0.29
2	10.3	0.29	0.71
3	5.3	0.72	0.28

rates; hole doping has been observed upon air exposure [28]. Unintentional adsorption of the reactive gases like O_2, NO_2, CO_2, H_2, and O can give rise to severe instabilities; this behavior of multiple absorption is detected by the algorithm and can be seen in the figure S24 on SI for O(1s), Zn(2p), and C(1s) spectra. Additionally with criterion of doublet separation (DS-2p) in the zinc analysis and extracting this difference of binding energies by descriptive method in mean peaks, see SI tables S10 and S8, there was a transition of the ZnO matrix, Δ (22.9, 23.0, 23.0 eV), to a matrix Al_2ZnO_4, Δ (23.1, 23.1, and 23.1 eV) [29] for samples 1,2, and 3, respectively.

The values detected by applying Riemannian distance for Al(2p) element on the surface yield binding energy values of 73.58 eV for samples 1 and 2 which correspond to an oxidation phase γ-Al_2O_3 [29]; while for samples 1 and 2 in etching, the binding energy was 73.28 eV and 73.48 eV respectively which correspond to Al in metallic phase [5, 30]. The peaks behavior before and after the etching does not present a distinguishable symmetry in the Al(2p) spectra due to the small number of Al_2O_3 incorporated in the ZnO:Al matrix [6]. However, the high sensitivity of the Riemannian distance was able to detect this specimen in the O(1s) spectra at a binding energy of 528 eV as you can see in SI figure S22.

4 Conclusions

AZO samples 1, 2, and 3 were fitting by Drude model where solutions obtained for perfect absorption at radiations (wavelengths) from 1244.5 nm, 1169.5 nm, and 929.5 nm yields the correspondings thicknesses in subwavelengths (λ_{ENZ}/100) at 16.9 nm, 23.2 nm, and 12 nm via the condition of critical coupling (ENZ mode) for a reference incidence angle at 44.2°.

A new method for spectroscopy analysis is proposed in the context the shape theory. The technique detects automatically elusive XPS peaks and avoids the use of classical fitting models. Inference and relate aspects about associated parametric models will be part of a future investigation.

Funding This study was funded by SEP PROFIDES project Materials for Alternate Energies.

Compliance with ethical standards

Conflict of interest A. L. V. R received research Grants from CONACYT-México (Grant # 15232). This work is the result of a multidisciplinary collaboration where A. L. V. R and M. G. M carried out the manufacture of the AZO films and the characterization tests (UV–VIS, XRD, and XPS). Professor F. J. C. L and his Ph.D. student F. O. P. R implemented the statistical theory for the samples classification and the automatic detection of the peaks from XPS data. Professor U. O. M collaborated in the financing of a project and revision of the manuscript. Original idea and first draft of the document was directed by Á. H. B. C along with the optical, morphological, and chemical characterizations.

Ethical standard This work complies with ethical standard.

References

1. Naik GV, Kim J, Boltasseva A (2011) Oxides and nitrides as alternative plasmonic materials in the optical range [Invited]. Opt Mater Express 1(6):1090. https://doi.org/10.1364/ome.1.001090
2. Aleksei A, Long T, Catherine A, Howard LHW (2018) Field-effect tunable and broadband epsilon-near perfect absorbers with deep subwavelength thickness. ACS Photon 5(7):2631. https://doi.org/10.1021/acsphotonics.7b01373
3. Zhai CH, Zhang RJ, Chen X, Zheng YX, Wang SY, Liu J, Dai N, Chen LY (2016) Effects of Al doping on the properties of ZnO thin films deposited by atomic layer deposition. Nanoscale Res Lett. https://doi.org/10.1186/s11671-016-1625-0
4. Anopchenko A, Gurung S, Tao L, Arndt C, Lee HWH (2018) Atomic layer deposition of ultra-thin and smooth Al-doped ZnO for zero-index photonics. Mater Res Express 5(1):014012. https://doi.org/10.1088/2053-1591/aaa653
5. Lin YC, Chen TY, Wang LC, Lien SY (2012) Comparison of AZO, GZO, and AGZO thin films TCOs applied for a-Si solar cells. J Electrochem Soc 159(6):H599. https://doi.org/10.1149/2.108206jes
6. Cho J, Yoon KH, Oh MS, Choi WK (2003) Effects of H2 annealing treatment on photoluminescence and structure of ZnO:Al/Al_2O_3 grown by radio-frequency magnetron sputtering. J Electrochem Soc 150(10):H225. https://doi.org/10.1149/1.1602458
7. Bedoya-Calle Á, García-Méndez M, Torres-Castro A, Shaji S, Ortiz-Méndez U (2015) Chemical characterization of DC-sputtered In_2O_3 films with a top SnO_2 layer. J Nano Res 30:86. https://doi.org/10.4028/www.scientific.net/JNanoR.30.86
8. Wang FH, Chang HP, Tseng CC, Huang CC (2011) Effects of H2 plasma treatment on properties of ZnO: Al thin films prepared by RF magnetron sputtering. Surf Coat Technol 205(23):5269. https://doi.org/10.1016/j.surfcoat.2011.05.033
9. Lehraki N, Aida M, Abed S, Attaf N, Attaf A, Poulain M (2012) ZnO thin films deposition by spray pyrolysis: influence of precursor solution properties. Curr Appl Phys 12(5):1283. https://doi.org/10.1016/j.cap.2012.03.012
10. Fernandes GE, Kim JH, Xu J (2017) Sol–gel synthesis and thermoelectric properties of AZO films with pyrolytic carbon inclusions. Superlattices Microstruct 109:161. https://doi.org/10.1016/j.spmi.2017.04.044
11. Chaves M, Ramos R, Martins E, Rangel EC, da Cruz NC, Durrant SF, Bortoleto JRR (2019) Al-doping and properties of AZO thin films grown at room temperature: sputtering pressure effect. Mater Res. https://doi.org/10.1590/1980-5373-mr-2018-0665
12. Kim H, Osofsky M, Prokes SM, Glembocki OJ, Piqué A (2013) Optimization of Al-doped ZnO films for low loss plasmonic materials at telecommunication wavelengths. Appl Phys Lett 102(17):171103. https://doi.org/10.1063/1.4802901
13. Prieto-Cortés P, Álvarez-Tamayo RI, García-Méndez M, Durán-Sánchez M (2019) Lossy mode resonance generation on sputtered aluminum-doped zinc oxide thin films deposited on multimode optical fiber structures for sensing applications in the 1.55 μm wavelength range. Sensors 19(19):4189. https://doi.org/10.3390/s19194189

14. Sherwood PM (2019) The use and misuse of curve fitting in the analysis of core X-ray photoelectron spectroscopic data. Surf Interface Anal 51(6):589. https://doi.org/10.1002/sia.6629
15. Caro-Lopera FJ, Díaz-García JA, González-Farías G (2010) Non-central elliptical configuration density. J Multivar Anal 101(1):32. https://doi.org/10.1016/j.jmva.2009.03.004
16. Quintero J, Mariño A, Šiller L, Restrepo-Parra E, Caro-Lopera F (2017) Rocking curves of gold nitride species prepared by arc pulsed—physical assisted plasma vapor deposition. Surf Coat Technol 309:249. https://doi.org/10.1016/j.surfcoat.2016.11.081
17. Ellmer K, Klein A, Rech B (2008) Transparent conductive zinc oxide: basics and applications in thin films solar cells. Springer series in materials science, vol 104. Springer, Berlin
18. Wood DL, Nassau K (1990) Optical properties of gadolinium gallium garnet. Appl Opt 29(25):3704. https://doi.org/10.1364/AO.29.003704
19. Raether H (1988) Surface plasmons on smooth and rough surfaces and on gratings. Springer tracts in modern physics. Springer, Berlin
20. Anopchenko A, Lee HWH (2017) In: Conference on Lasers and Electro-Optics (Optical Society of America, 2017), p. JTh2A.94. https://doi.org/10.1364/CLEO_AT.2017.JTh2A.94
21. Albertsson J, Abrahams SC, Kvick A (1989) Atomic displacement, anharmonic thermal vibration, expansivity and pyroelectric coefficient thermal dependences in ZnO. Acta Crystallogr Sect B Struct Sci 45(1):34. https://doi.org/10.1107/s0108768188010109
22. García-Méndez M, Segura RR, Coello V, Martínez Guerra E, Bedoya-Calle Á (2015) The influence of Ce doping on the structural and optoelectronic properties of RF-sputtered ZnO films. Opt Quantum Electron 47(8):2637. https://doi.org/10.1007/s11082-015-0145-y
23. ÁH BC (2015) Fabricación y caracterización de películas delgadas de óxidos transparentes con aplicaciones ópticas. Ph.D. thesis, FIME-UANL. http://eprints.uanl.mx/id/eprint/10992
24. Prabhu YT, Rao KV, Kumar VSS, Kumari BS (2014) X-ray analysis by williamson-hall and size-strain plot methods of ZnO nanoparticles with fuel variation. World J Nano Sci Eng 04(01):21. https://doi.org/10.4236/wjnse.2014.41004
25. Rogers K, Daniels P (2002) An X-ray diffraction study of the effects of heat treatment on bone mineral microstructure. Biomaterials 23(12):2577. https://doi.org/10.1016/s0142-9612(01)00395-7
26. Cullity BD, Smoluchowski R (1957) Elements of X-ray diffraction. Phys Today 10(3):50. https://doi.org/10.1063/1.3060306
27. Turner NH (1992) Estimates of peak areas and relative atomic amounts from wide-scan XPS spectra. Surf Interface Anal 18(1):47. https://doi.org/10.1002/sia.740180108
28. Panchal V, Giusca CE, Lartsev A, Martin NA, Cassidy N, Myers-Ward RL, Gaskill DK, Kazakova O (2016) Atmospheric doping effects in epitaxial graphene: correlation of local and global electrical studies. 2D Mater 3(1):015006. https://doi.org/10.1088/2053-1583/3/1/015006
29. Strohmeier BR, Hercules DM (1984) Surface spectroscopic characterization of the interaction between zinc ions and γ-alumina. J Catal 86(2):266. https://doi.org/10.1016/0021-9517(84)90372-5
30. Moulder J, Chastain J (1992) Handbook of X-ray photoelectron spectroscopy: a reference book of standard spectra for identification and interpretation of XPS data. Perkin-Elmer Corporation, Physical Electronics Division